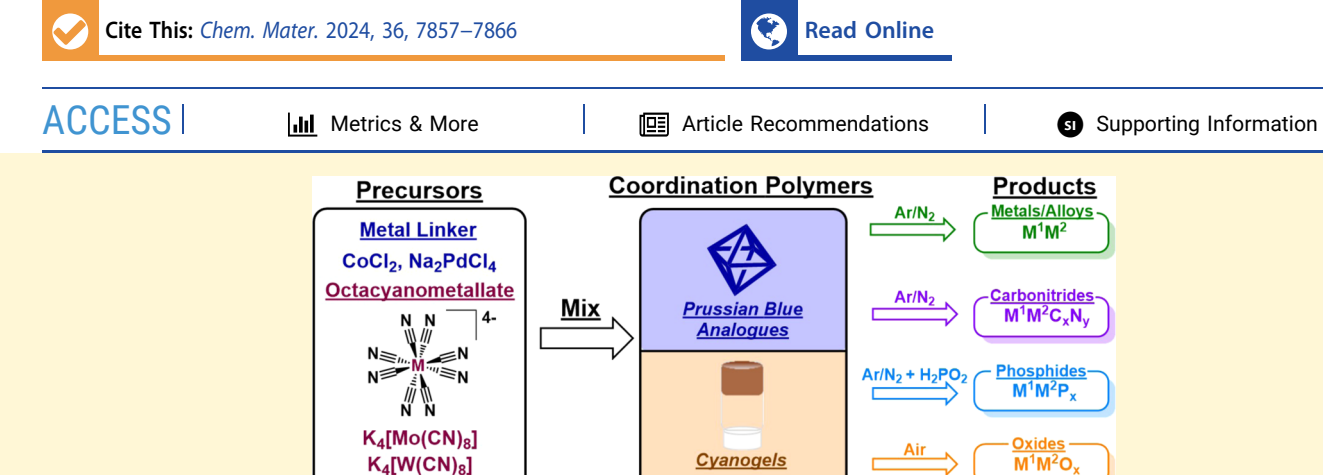


pubs.acs.org/cm Article

Extending Cyanogel and Prussian Blue Analogue Chemistry to Octacyanometallate-Based Coordination Polymers: Reduced Temperature Routes to Materials Based on Molybdenum and Tungsten

Josef A. Lawrence, Stephanie Dulovic, Kai A. Filsinger, Scott B. Lee, and Andrew B. Bocarsly*



ABSTRACT: Cyanide coordination polymers (CCPs) and their products made via thermolysis make up a promising class of materials for a variety of energy and analytical applications. While the chemistry of hexacyanometallate-based CCPs is well developed, that of their octacyanometallate $[M(CN)_8]^{4-}$ (M=Mo,W) analogues is underexplored. This work compares the synthesis, morphology, and thermolytic properties of two types of cyanide coordination polymers: the amorphous $[PdCl_4]^{2-}$ -based cyanogel, Pd-Mo/W, and the nanocrystalline $CoCl_2$ -based Prussian blue analogue, Co-Mo/W. The general decomposition pathways and products for $[M(CN)_8]^{4-}$ -containing polymers are comparable to their hexacyanometallate analogues. All four coordination polymers can be converted to mixed oxide and ternary phosphide systems and generally retain morphology upon heating. Notably, the reduction under inert gas generates alloys in the cyanogel systems and complex reduced mixtures in the Prussian blue analogue (PBA) systems.

Low Temperatures

INTRODUCTION

Despite a history spanning over 300 years, cyanide coordination polymers (CCPs) and CCP-derived materials continue to be the subject of intense research interest due to their promising applications in numerous fields, including materials chemistry, sensors, batteries, and catalysts. ¹⁻¹⁵ These compounds, which include the Prussian blue analogues (PBAs), are characterized by the coordination of the N-terminus of a cyanide ligand with an additional metal center to generate a bridging cyanide (M−C≡N−M) moiety. When the linking metal is able to coordinate multiple cyanides, these linkages can extend and generate a framework of bridging cyanides (Figure 1).

Straightforward Synthesis

By their nature, these compounds have metals that are atomically dispersed in well-established coordination environments. By modifying auxiliary ligands and recrystallization conditions, these frameworks can extend as chains, ribbons, sheets, and other structures. The tendency of CCPs to generate defect-rich structures results in highly porous

materials with a significant surface area-to-volume ratio. This ability to accommodate defects also allows for variation in the linker-cyanometallate ratio and for some cyanide ligands to be replaced by other ligands with minimal change in the overall structure. This tunability of both the atomic- and macroscale environments give CCPs properties reminiscent of both homogeneous metal coordination complexes and metal—organic frameworks. By mixing multiple metal linkers in addition to the cyanometallate, binary, ternary, and higher-order multimetallic species can be synthesized. All things

Retained Morphology

Received: April 24, 2024 Revised: July 23, 2024 Accepted: July 24, 2024 Published: August 8, 2024





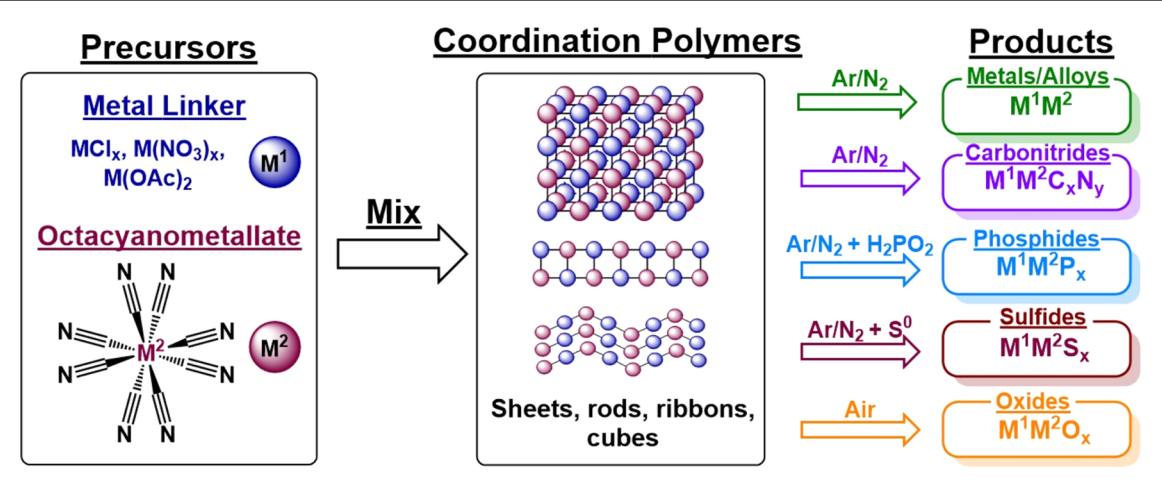


Figure 1. Overview of the synthesis and potential thermolytic products for CCPs.

considered, these factors make CCPs an incredibly flexible and modular platform for materials design.

CCPs are also notable for their ability to be converted to a variety of inorganic solids. Thermolysis of CCPs under inert gas causes the reductive elimination of cyanogen, resulting in the formation of a variety of products, including metal alloys, carbides, and nitrides. These products can be modified with the addition of volatile compounds upstream during thermolysis, such as elemental sulfur or phosphine gas, to generate metal sulfides and phosphides, respectively. Calcination under air results in metal oxides. These converted structures generally retain the bulk morphology of the parent CCP.

One distinct subclass of CCPs is a group of hydrogels known as cyanogels. These materials form from the reaction of cyanometallates and noble or p-block metal halides (e.g., PdCl₄²⁻, RuCl₃, InCl₃, PtCl₄²⁻, etc.). PdCl₄²⁻ Upon mixing aqueous solutions, a framework forms that spans the entire solution volume; the resulting gelatinous material is >95% water by weight. Unlike microcrystalline PBAs, which frequently precipitate instantaneously upon mixing solutions, cyanogel hydrogels often take hours or even days to form and are amorphous. The mechanism of CCP formation, namely, via bridging cyanides, is identical, but the reaction rates vary considerably. Upon dehydration, the pore structure of the hydrogel collapses to generate xerogels. Similar to PBAs, cyanogel xerogels can be calcined to form alloys and oxides with a variety of morphologies depending on the preparation method and annealing temperature. 30,34

Cyanometallates can be generated with a variety of ligand geometries, such as the octahedral $[M(CN)_6]^{n-}$, square planar $[M(CN)_4]^{n-}$, and the much less common square prismatic $[M(CN)_8]^{n-}$. Octacyanometallate $[M(CN)_8]^{n-}$ (M = Mo, W, Nb)-based coordination polymers have been synthesized before in the context of molecular magnetism and materials science. To the best of our knowledge, there are no reports of $[M(CN)_8]^{n-}$ -derived cyanogels and few reports of $[M(CN)_8]^{n-}$ CCP-derived materials, with products solely focusing on oxides. $^{36-39}$

One notable aspect of CCP-thermolysis chemistry is that the reaction temperatures needed to produce solid-state products are far below the melting points of the pure metal components. This is particularly advantageous for synthesis involving Mo- or W-based compounds, given that molybdenum and tungsten are notable refractory materials. Conventional solid-state

reactions often involve the melting of all precursors; developing this reaction space could give access to a variety of multimetallic systems containing Mo and W, which are not available by using traditional methods.

In this work, we report on the potential for $[Mo(CN)_8]^{4-}$ and $[W(CN)_8]^{4-}$ to be used as synthons for both microcrystalline and amorphous CCPs and, thereby, their thermally derived solid-state products. To this end, we explore the chemistry of two sample materials, Co–Mo/W and Pd–Mo/W, including their conversion to a variety of materials, including oxides, alloys or carbonitrides, and phosphides. Here, we show that while all four systems studied retain their morphology upon thermolysis and all are capable of forming metal oxides under air, only the cyanogel forms can generate Mo and W alloys under inert gas conditions. We additionally demonstrate the successful formation of Mo- and W-containing phosphides.

■ EXPERIMENTAL SECTION

General. Unless noted, all water used was Milli-Q ultrapure water (18.2 $M\Omega$) from Sigma-Aldrich. Alumina crucibles were obtained from Thomas Scientific. All commercially available compounds were used without further purification.

Synthesis of $K_4[M(CN)_8]$. $K_4[Mo(CN)_8]$ and $K_4[W(CN)_8]$ were synthesized according to previous literature procedures. WBH₄ (>98%) and Na₂MoO₄ (>98%) were purchased from Sigma-Aldrich. KCN (97+%) was purchased from Alfa Aesar. Glacial acetic acid was obtained from Fisher Chemical. Na₂WO₄ (reagent grade) was obtained from Baker & Adamson. Animal-activated charcoal was purchased from Sigma-Aldrich. These salts were purified via filtration of an aqueous solution through Celite and precipitation with MeOH. The purity of these compounds was confirmed via IR before use (Figure S1). The resulting yellow solids are air- and water-stable and can be stored in the dark for extended periods of time.

Synthesis of Co–Mo/W PBAs. $CoCl_2 \cdot 6H_2O$ was obtained from Alfa Aesar. PVP (55,000 mw average) was obtained from Sigma-Aldrich. The synthesis of these compounds was adapted from a literature procedure.³⁷ To a beaker was dissolved $K_4[M(CN)_8]$ (0.2 mmol) in ~120 mL of Milli-Q water to form a clear, yellow solution and warmed to ~30 °C in a water bath. In a separate beaker, $CoCl_2 \cdot 6H_2O$ (4 mmol, 96 mg, 2 equiv) and 4 g of PVP (1 g/0.1 mmol Co) were dissolved in ~120 mL of Milli-Q water. The Co solution was then added portionwise using a pipet to the $K_4[M(CN)_8]$ solution with stirring and then allowed to stir for 1 h. The solution slowly turned cloudy, and the solid began to settle on the bottom. Acetone (~40 mL) was then added to further precipitate the solid. This suspension was then centrifuged at 7500 rpm for 10 min to separate the solid. The solution was decanted off, and the solid was

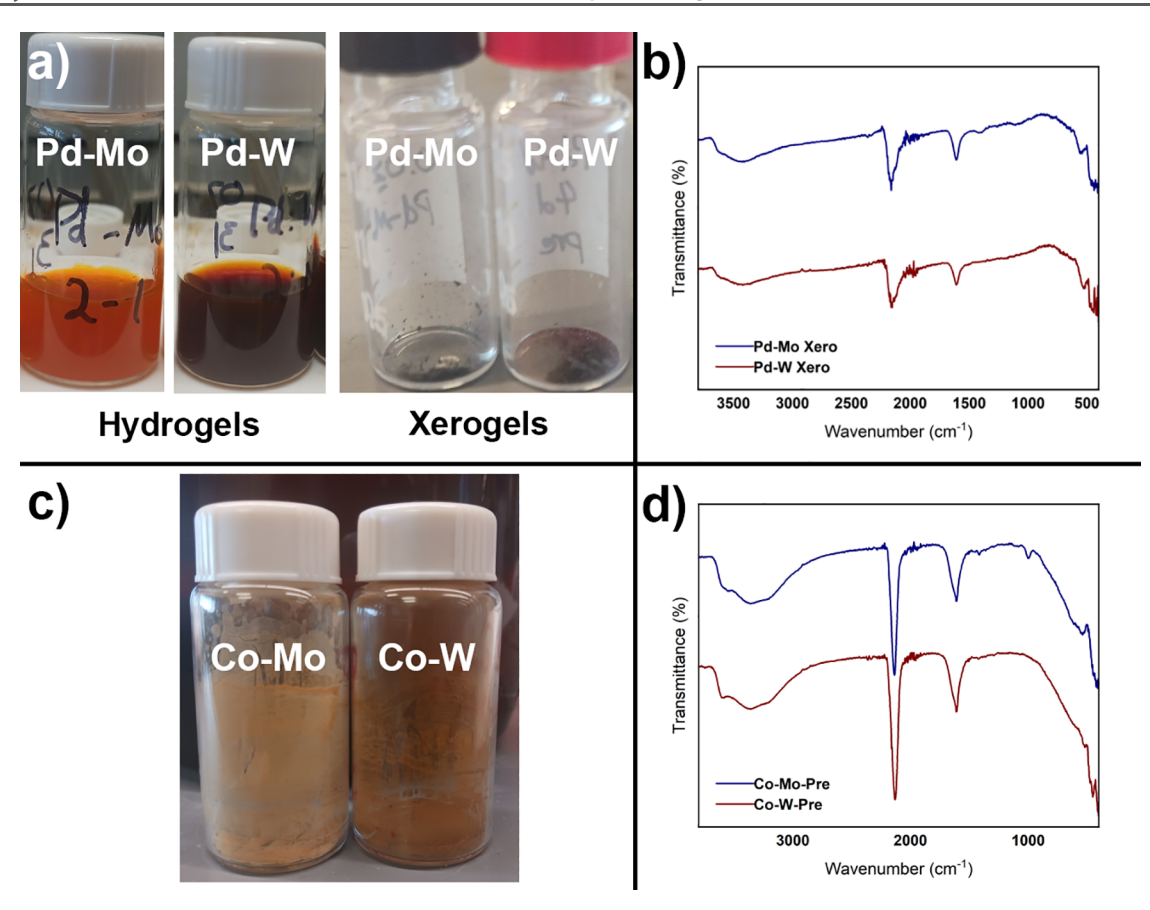


Figure 2. Images and IR spectra of Pd-Mo and Pd-W (a, c) and Co-Mo and Co-W (c, d).

resuspended in ethanol and centrifuged again. Care should be taken not to apply force to this solid via strong pipetting or shaking, as the solid may not resettle during centrifugation. This rinsing procedure was repeated. Finally, the solid was finally transferred to a vial and allowed to dry to yield a fine powder.

Synthesis of Pd–Mo/W Cyanogels. To a volume of 50 mM solution of $K_4[M(CN)_8]$ was added twice the volume of 50 mM PdCl $_4$ solution for a 2:1 Pd:M molar ratio. The color changes immediately upon mixing. The solution is gently swirled and then allowed to stand without stirring for at least 2 h. During this time, the liquid converts to an orange-brown gelatinous solid. This gel is then scooped out, spread onto filter paper, and allowed to air-dry in a fume hood overnight. The dark red-brown xerogel granules are then scraped off the filter paper and collected.

Thermal Processing. CCPs were placed in alumina crucibles and heated in a programmable Thermo Scientific Lindberg/Blue M 1200C furnace under Ar at a flow rate of 10 mL/min. Samples were heated at a rate of 3 °C/min to the desired temperature, maintained for 2 h, and cooled down to room temperature. To generate alloys and phosphides, a flowing argon atmosphere was used. For inert gas conditions, granules of the Zr (Alfa Aesar, 99.5% Zr/Hf) sponge were placed upstream in an alumina crucible to help scavenge oxygen. For phosphides, an alumina boat was filled with Na₂H₂PO₂ upstream to generate PH₃ in situ. To generate oxides, compressed air was used for gas flow. CAUTION! Toxic gases (CN)₂, HCN, and PH₃ may evolve during heating. PH₃ and cyanogen are pyrophoric and will burn in air to make a flame. The furnace was placed in a fume hood with the sash closed. After passing through an oil bubbler, the exhaust was also bubbled through a solution containing concentrated NaOCl to quench products.

Characterization. FTIR analysis was performed on solids using a Thermo Scientific Diamond Smart Orbit IR Spectrometer. X-ray diffraction (XRD) patterns were obtained by using the Debye–Scherrer method on a STOE STADI P diffractometer with a Mo K α radiation source (λ = 0.71073 Å) and graphite monochromator. The

samples were ground and adhered between two pieces of clear (Scotch) tape. A blank for the tape was generated as a background and subtracted from the samples to generate the final reported data. The measurements were taken over the interval $2\theta = 6-42^{\circ}$ in 6 overall steps with 480 s per step. Peak matching was done using the Powder Diffraction File (PDF) database using the STOE WINXPOW Search/Match PDF Program. A list of PDFs with the best alignment is included in the Supporting Information. The atomic ratios of the xerogels and reduced products were examined using scanning electron microscopy (SEM) and energy-dispersive X-ray analysis (EDX). SEM and EDX images were taken using a Verios 5 XHR SEM with corresponding EDX attachment and examined with AZtec software. EDX measurements were performed on 4–6 distinct regions of the SEM image, and the reported values are the average of those sites.

Thermogravimetric analysis was performed using a PerkinElmer TGA-8000 with a connected PE Clarus 680 gas chromatograph and SQ8T Mass Spectrometry system. TGA measurements were performed under nitrogen.

RESULTS AND DISCUSSION

Precursor Synthesis and Characterization: Pd–Mo/W and Co–Mo/W Coordination Polymers. Previous research in our group focused on understanding the chemical and thermolytic properties of cyanogels through the model system of Na₂PdCl₄ + K₃[Co(CN)₆], abbreviated herein as Pd–Co. To this effect, we chose to use Na₂PdCl₄ as our linker for exploring $[M(CN)_8]^{n-}$ -based cyanogel chemistry. Furthermore, since previous Pd–Co research from our group and previous reports on Co–Mo and Co–W oxides both use 2–1 stoichiometry, we chose this ratio for this work. Co was chosen due to ease of comparison with the established literature involving Co–Mo(CN)₈-derived oxides.

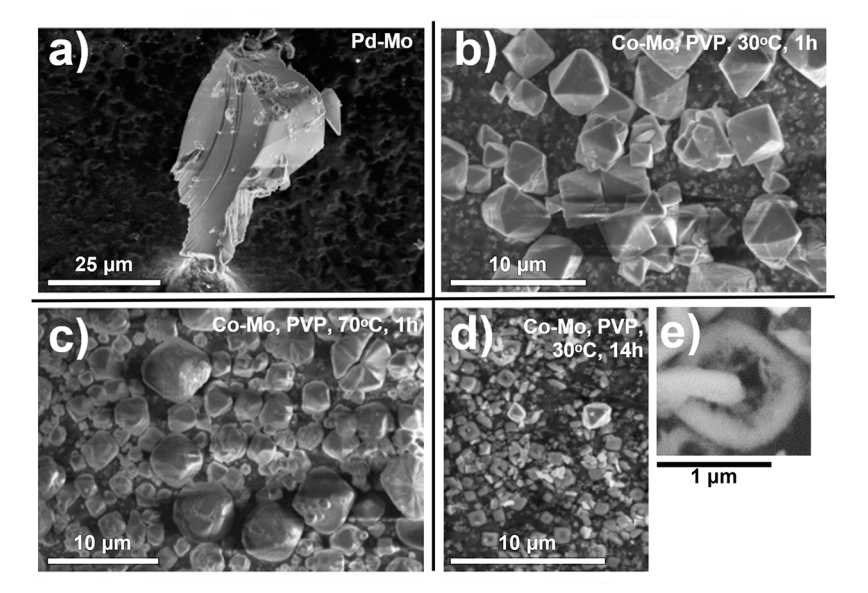


Figure 3. SEM images of [Mo(CN)₈]⁴⁻-based coordination polymers (a) Pd-Mo and (b-e) Co-Mo having a variety of morphologies.

Upon mixing solutions of Na₂PdCl₄ and K₄[M(CN)₈], the orange-brown liquids eventually solidified to form gelatinous solids that spanned the entire reaction volume. Removing the water from this gel resulted in small granules that could not be rehydrated upon treatment with water (Figure 2a). IR analysis of the xerogel demonstrates peaks at 2150, 1600, and 3300–3400 cm⁻¹. The 2150 cm⁻¹ peak is consistent with the presence of bridging cyanides, while the remaining peaks indicate the incorporation of water (Figure 2b). EDX analysis for these compounds identified Pd, Mo/W, C, N, and O, along with variable amounts of NaCl/KCl trapped in the xerogel network. EDX mapping showed that these elements are homogeneously dispersed in the xerogel (Figure S2). SEM imaging revealed amorphous granules that can fracture to form jagged edges (Figure 3a).

For the PBA system, the slow addition of the PVP-ligated Co solution to the $[M(CN)_8]^{4-}$ solution led to the slow formation of a cloudy solution. Precipitation of this powder generated a nanocrystalline solid (Figure 2C). IR analysis of these materials showed cyanide stretching frequencies in the same region as the Pd-Mo system, indicative of the presence of bridging cyanides (Figure 2D). The Co-Mo coordination polymers can adopt a variety of morphologies, including hollow loops, octahedra, and grain-like ellipses (Figure 3b-e). The morphology is sensitive to several factors, including the stirring time, PVP amount, and solution concentration. Consistent control of these parameters is critical for ensuring the desired morphology. Stirring overnight results in more varied morphologies. (Figure 3d). Co-W is shown to have similar variations as the Co-Mo system (Figure S6). Octahedra generally varied from 250 nm to 2 μ m. Unlike the cyanogel system, EDX analysis of Co-Mo and Co-W was shown to have a near absence of chlorine. Both metals are evenly dispersed throughout samples based on SEM/EDX mapping (Figure S3). The degree of crystallinity is largely dependent on the overall rate of bridging cyanide formation with distinct steps involving chloride loss and M-NC bond formation. In the Co-based systems, Cl⁻ loss is fast, and thus, the rate is dependent on the reaction of $[Co(H_2O)_6]^{2+}$ with the cyanometallate. Without PVP, precipitation is immediate and leads to a poorly crystalline material. The addition of PVP

slows the rate of formation, leading to improved crystallinity. For cyanogel systems, the rate of Cl⁻ loss from the chlorometallate is rate-limiting and sufficiently slow that M–NC formation occurs evenly throughout the solution and slowly develops into a hydrogel.

Thermolysis and Derivatization under Inert Gas: Differences in Product Speciation. Analyzing the thermolytic behavior of the 2–1 Pd–Mo/W xerogels via TGA revealed a pattern similar to those seen in the Pd–Co system and was characterized by four key events: (1) Initial water loss at 60–110 °C, (2) minor mass loss beginning at ~200–220 °C, (3) major loss beginning at ~400 °C, and (4) slow but accelerating loss at temperatures >650 °C (Figure 4).

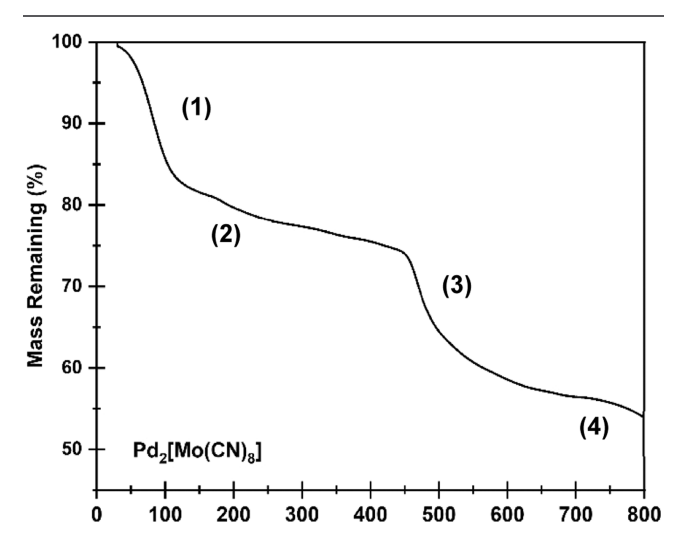


Figure 4. TGA spectrum of Pd-Mo under nitrogen.

There is a 5.0% mass loss from 150 to 400 °C. This loss is associated with the dissociation of cyanide and corresponds to a range of 0.72–1.02 CN⁻ lost per Pd atom (see the Supporting Information (SI) for sample calculations). Between 400 and 525 °C, 18.7% of the sample mass is lost, consistent with the loss of between 2.65 and 3.71 CN⁻ per Pd atom. This implies that similar to the Pd–Co system, bridging CN⁻

ligands are lost first to reduce the Pd.²⁹ The third mass loss involves reductive elimination of the remaining 6 cyanide ligands from the octacyanometallate to generate a reduced species. Finally, above 600–700 °C, residual NaCl/KCl from the ligand exchange reactions begins to sublime out of the system. TGA analysis of the Co-based systems under nitrogen showed curves with the same general structure with the exception of masses stabilizing beyond 600–700 °C. This is consistent with the lack of alkali halide salts in Co–Mo/W compared to the cyanogel analogues. For both the Co–W and Pd–W systems, the temperature required for reductive elimination during the third mass loss is shown to be approximately 100 °C higher than those of the molybdenum analogues (Figures S7–S9).

After performing TGA to gain insight into the chemistry and help determine the optimal thermolysis temperature, the precursors were thermolyzed at a variety of temperatures, with the disappearance of the cyanide IR stretch being used as a handle for determining reaction completeness. Treatment of Pd–Mo and Pd–W cyanogels at temperatures between 400 and 700 °C led to the total disappearance of cyanide stretches while they were still present at 300 °C (Figure S10). Thus, an initial thermolysis temperature of 400 °C was chosen. However, for the Co-based systems, the powder formed at these temperatures was shown to be poorly crystalline. Reduction at 700 °C generated considerably more crystalline material (Figure 5).

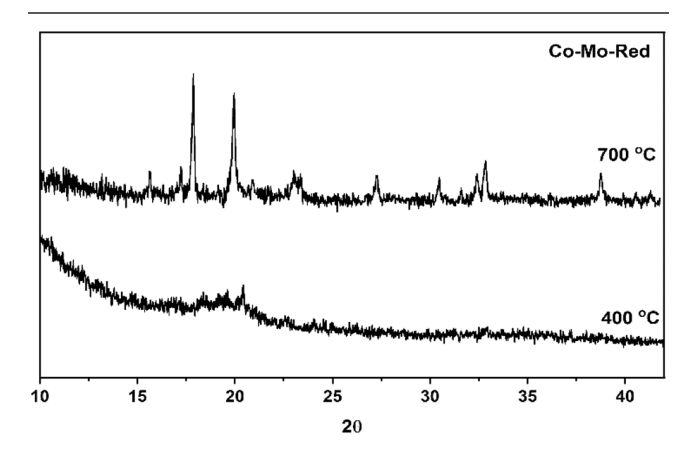


Figure 5. Comparison of XRD spectra of Co–Mo thermolyzed under argon at 700 $^{\circ}$ C (top) and 400 $^{\circ}$ C (bottom).

IR analysis of both the reduced Pd–Mo/W and Co–Mo/W product mixtures (abbreviated henceforth as Pd–Mo–Red and Co–Mo–Red) confirmed the loss of all features consistent with cyanides; this was corroborated by the disappearance of the nitrogen peak in the EDX spectra (Figure S11). Generally speaking, ratios determined by EDX were found to be comparable to those of the initial precursor. For the Pd-based system, the presence of an oxygen scavenger was found to be critical for maintaining proper stoichiometry. The morphology for all four systems is maintained after thermolysis (Figure 6). The Co-based systems retain their octahedral shape but appear to have rougher surfaces.

XRD analysis of these materials indicates a difference in reactivity when comparing the Pd- and Co-based systems. The cyanogel systems generated predominantly elemental palladium and palladium-Mo/W alloys, both of which are isostructural in a face-centered cubic (FCC) lattice. Addition-

ally, molybdenum carbide β -Mo₂C and tungsten semicarbide are seen respectively as minor products (Figure S17). EDX analysis of these samples demonstrates distributed products with both Pd and Mo/W present, confirming the formation of a multiphasic mixture consisting of Pd and Pd/M solid solutions. In the case of the Co–Mo/W systems, the two predominant components were elemental cobalt in an FCC lattice along with metal carbide (Figure S18). Notably, the predominant allotrope of tungsten carbide in Co–W–Red is WC as opposed to Mo₂C identified in Pd–Mo–Red. Given that the only source of carbide is the cyanide and both systems have similar TGA data, this implies that some metal–metal interaction takes place before complete reductive elimination of cyanide ligands, thus controlling the ratio of Mo⁰/W⁰ vs carbide formation.

Proposed Mechanism of Alloy Formation. Based on our prior work involving Pd-Co cyanogel, as well as the observed similarity of the TGA data between Pd-Mo and Pd-Co, we hypothesize a similar reduction mechanism for both systems. 29,30,42 Namely, heating above 200 °C results in the transfer of two equivalents of CN- to the linking metal to generate, e.g., Pd(CN)₂ or Co(CN)₂. Subsequent reductive elimination of cyanogen generates a zerovalent linker species. Previous analysis on the decomposition of Prussian blue demonstrates the formation of metallic iron and iron carbide, with cyanogen and dinitrogen as gaseous products when heated at temperatures comparable to those used here.⁴³ Similar reactivities are reported for many other PBAs. In contrast, previous reports indicate the formation of alloys from Sn-Fe, Pt-Co, Ru-Pd, Pd-Co, Pd-Cu, and Pd-Fe cyanogels. Given that similar cyanometallates like [Co-(CN)₆]³⁻ were used in both cases, it is likely that the product distribution is more of a function of the linking metal rather than the cyanometallate. 33,44,45

Interestingly, it is reported that $K_2[Pt(CN)_4]$ and $K_2[Pt-$ (CN)₄Br₂] form Pt metal, KCN, and (CN)₂ upon thermolysis under Ar.46 After reduction, Pt0 would rather perform ligand release of CN- than further chemistry. Furthermore, the reduction of Pt(IV) was demonstrated to proceed via a step containing Pt(III) with cyanide bridging centers. 46 This is consistent with our finding that bridging cyanides tend to promote the reduction of the metal centers over ligand loss or cyanide C-N cleavage. Given these factors, we propose that there are likely a variety of potential mechanisms that, taken together, explain alloy formation and metal carbide suppression. One mechanism involves catalytic reduction of the cyanometallate by Pd via a mechanism of cyanide transfer, reductive elimination of (CN)₂, electron transfer from Pd to the other metal, and finally, cyanide transfer back to Pd (Scheme 1a). This would explain the lack of carbides present and the metallic state for the variety of 3d and 4d metals used as linkers. Alternatively, the reduction of the metal species could proceed via an outer-sphere-type mechanism involving cyanide radical formation and one electron charge transfer to the metals. These radicals could couple to form cyanogen, while charge transfer between the metal centers would produce the observed metallic compounds (Scheme 1b). The selectivity of alloy vs carbide would then vary with the nature of the bridging cyanide bond. Metals such as Pd, Ru, and Sn change the bond dissociation free energy of the M-CN bond to favor cyanide radicals over other potential pathways, with these alternative pathways giving rise to carbides and nitrides.

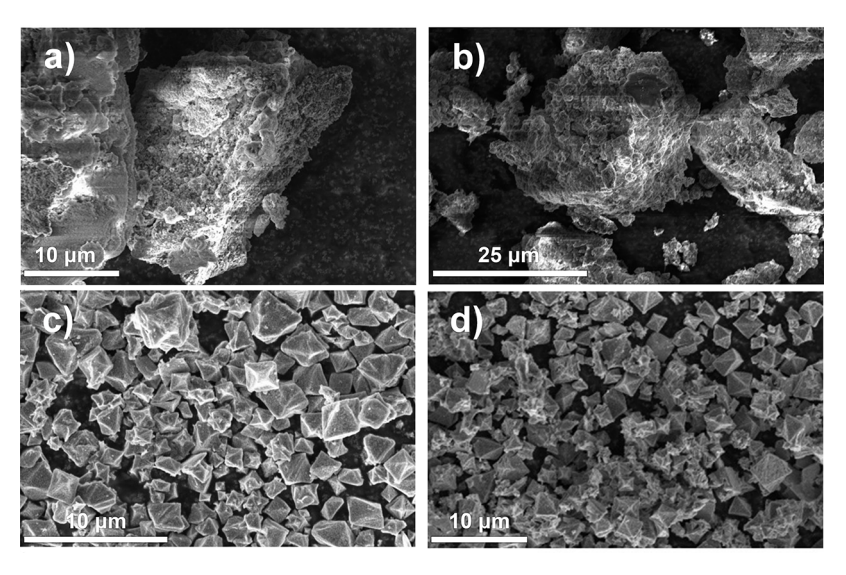
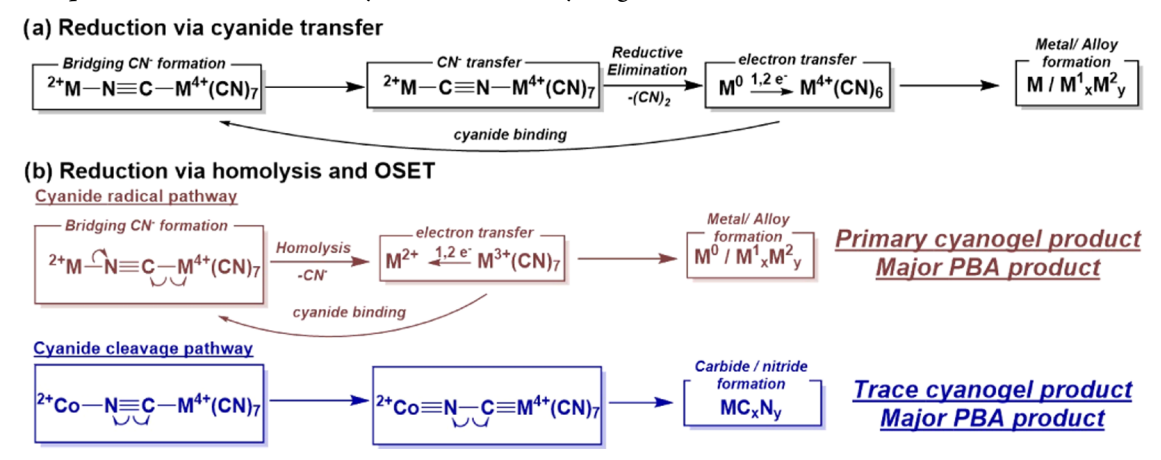


Figure 6. SEM image of products after thermolysis under argon (a) Pd-Mo-Red, (b) Pd-W-Red, (c) Co-Mo-Red, and (d) Co-W-Red

Scheme 1. Proposed Mechanisms for Alloy Formation for Cyanogel Reactions



Further Functionalization to Metal Oxides and Phosphides: Discrepancies to Product Ratios. To further compare the reactivity of the Pd-based and Co-based coordination polymers, the samples were treated under flowing air to generate metal oxides. As with the reduced materials, the oxides for all four systems retained morphology following thermolysis (Figures S19-S22). For the cyanogel systems, XRD analysis indicated the formation of PdO, with minor peaks suggesting a separate phase consistent with WO3 or MoO₃ (Figures S23 and S24). This implies either that these components disappear during thermolysis or that Mo/W is incorporated into the structure to form a bimetallic oxide. Inspection of these products with EDX showed a relative increase in the Pd to Mo/W ratio for both products, increasing to 74 and 71%, respectively (Figure S12). Given that the metal ratios for both Pd-W-Red and Pd-Mo-Red remain comparable to their original ratios, this implies that treatment in the presence of air can lead to the elimination of the $[M(CN)_8]^{4-}$ derived species. MoO₃ and WO₃ can become volatile above 600 °C. 47,48 Therefore, it is plausible that slow sublimation of these group 6 oxides results in a final product depleted in Mo or W. Despite the change in stoichiometry, SEM indicates essentially no change in bulk morphology. For the Co-based systems, XRD analysis of the molybdenum

sample indicated $CoMoO_4$ and Co_3O_4 to be the primary products, a result consistent with literature reports. ³⁷ In the W-derived system, $CoWO_4$ appeared to be the primary product with trace Co_3O_4 (Figures S23 snd S24). ³⁶ Despite Co-W-Ox appearing monophasic via XRD, SEM analysis indicates minor variations in metal ratios (Figure S12). Both spectra are comparable to those previously in the literature involving treatment at lower temperatures. Notably, the Co/M ratio is shown to remain comparable to those of both the precursor and the alloy. This implies that the reaction leading to the disappearance of Mo/W from the cyanogel system is suppressed during the formation of these metal oxides.

Metal phosphides derived from cyanide coordination polymers can be generated directly from the polymers themselves or from CCP-derived metal oxides. To this effect, two separate routes for the synthesis of phosphides were examined. For simplicity, the oxide- and coordination polymer-derived systems will be referred to as, e.g., $Co-Mo-P_{ox}$ and $Co-Mo-P_{CP}$, respectively. Following treatment with PH₃, all of the resulting compounds contained phosphorus according to EDX (Figure 7). Generally, oxide-derived phosphides had lower atomic percentage phosphorus than CCP-derived ones. Co-based systems had higher atomic% P, but there is no clear trend between Mo vs W. The metal final ratios were shown to

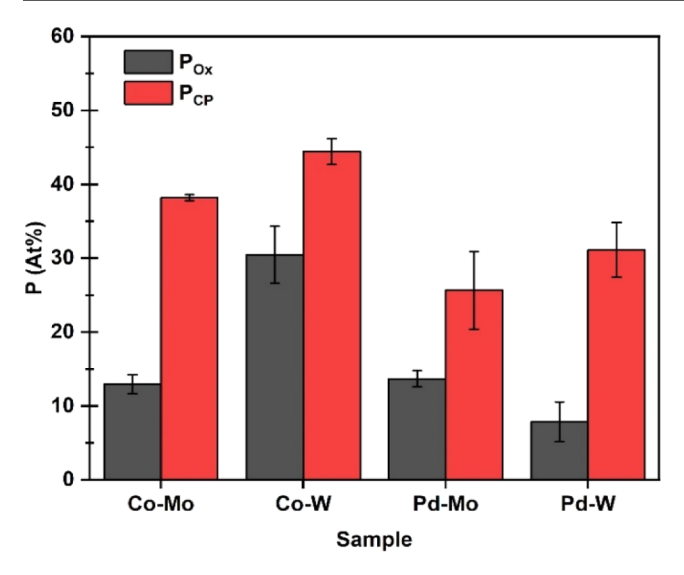


Figure 7. Comparison of phosphorus content over all metal phosphides studied.

be different as a function of the starting material when comparing oxide- and CCP-derived materials of the same elements. In the case of Pd-systems, oxides treated with phosphine were shown to have a higher percentage Pd. This is likely due to Mo/W disappearance during the oxide formation rather than during phosphidation. For all four systems, bulk morphology remained comparable for both the oxide (Figures S25–S28) and CCP-derived materials (Figures S31–S34).

XRD analysis of these structures showed an interesting discrepancy in the behavior between all systems. Both Pd-Mo-Pox and Pd-W-Pox showed the formation of elemental palladium and Pd-containing alloys, rather than phosphides, as the major components. These XRD peaks aligned exactly to those generated from the reduced species, with the exception of not having metal carbide. This is confirmed by an overall metal-to-phosphorus ratio M_{total}/P of less than 85:15 for both Pd-Mo-P_{ox} and Pd-W-P_{ox}. Furthermore, these samples demonstrated that no major peak correlated to metal phosphides for either system. This implies that phosphine predominantly reduces the oxides with a minor incorporation into the lattice. Furthermore, these phosphide patches are likely to have inconsistent stoichiometry and are too poorly crystalline to be detected via XRD. For the coordination of polymer-derived phosphines, phosphorus incorporation was significantly increased, with an average M/P ratio of greater than 75:25 for both. Individual spots for EDX analysis, however, had considerable variation in phosphorus quantity (Figure 7). XRD analysis of Pd-Mo-P_{CP} and Pd-W-P_{CP} showed poorly crystalline samples, with the metal carbide and metal nitride minor impurities as the most prominent peaks. When compared to the reduced species without phosphine, Pd-Mo-P_{CP} and Pd-W-P_{CP} lack the peaks corresponding to Pd⁰ and Pd-W alloy at 22, 30, and 35° (Figure 8). This implies that PH3 suppresses the formation of these species. Palladium phosphides are shown to have a large variation of peak positions as a function of stoichiometry. Given the significant phosphorus presence via EDX, we argue that the most likely composition of this material is a mixture of tungsten carbide, palladium nitride, and a multiphasic mixture of palladium phosphides. Pd-Mo-P_{CP} demonstrated comparable crystallinity and also had suppression of the Pd-Mo

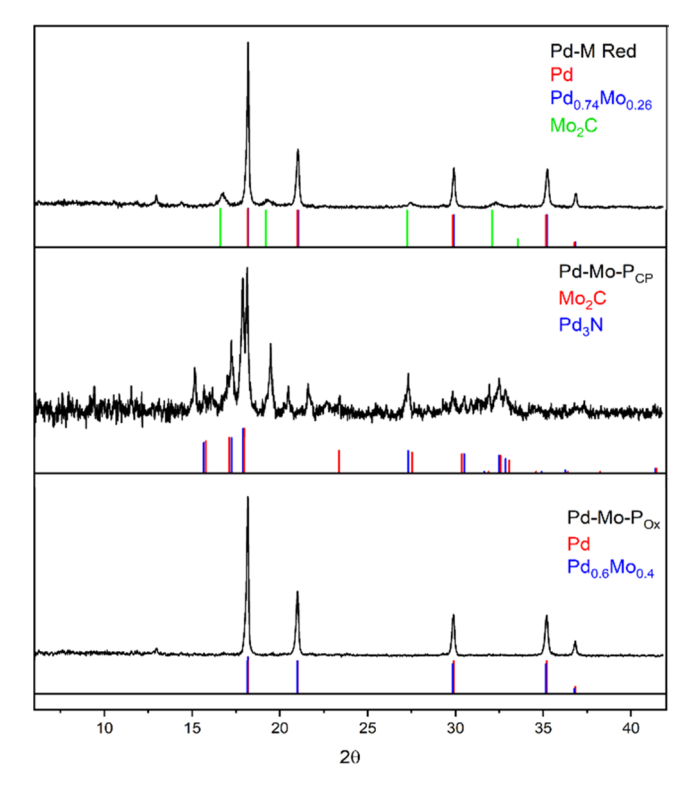


Figure 8. Proposed components and XRD Comparison of the Pd—Mo-derived phosphides and Pd—Mo alloy.

alloy. This system is also likely a heterogeneous mixture of phosphides as well. A summary of all major components can be found in Table 1, with a more exhaustive list located in the Supporting Information.

Table 1. Overview of Major Products for Each Material Examined in This Work

class	compound	major components
reduced materials	Co-Mo-Red	Co ⁰ , Mo ₂ C
	Co-W-Red	Co ⁰ , WC
	Pd-Mo-Red	Pd ⁰ , Pd _x Mo _y alloy, Mo ₂ C
	Pd-W-Red	Pd^0 , Pd_xW_y alloy, W_2C
oxides	Co-Mo-Ox	Co ₃ O ₄ , CoMoO ₄
	Co-W-Ox	CoWO ₄
	Pd-Mo-Ox	PdO
	Pd-W-Ox	PdO, WO ₃
CCP-derived phosphides	$Co-Mo-P_{CP}$	assorted Co_xMo_y P_z
	$Co-W-P_{CP}$	CoWP ₂
	$Pd-Mo-P_{CP}$	assorted $Pd_xMo_y P_z$
	$Pd-W-P_{CP}$	assorted Pd_xW_y P_z
oxide-derived phosphides	Co-Mo-P _{Ox}	residual oxide, assorted $\mathrm{Co}_x\mathrm{Mo}_y$ P_z
	Co-W-P _{Ox}	residual oxide, assorted Co_xW_y P_z
	$Pd-Mo-P_{Ox}$	Pd ⁰ , Pd _x Mo _y alloy
	$Pd-W-P_{Ox}$	Pd^0 , Pd_xW_y alloy

For the cobalt-containing materials, the results of phosphidation varied considerably between all four cases studied. XRD analysis indicates that the primary components of $Co-Mo-P_{ox}$ and $Co-W-P_{ox}$ are still oxides, with some potential peaks consistent with metal phosphides. The EDX, however, indicates significant phosphorus incorporation in

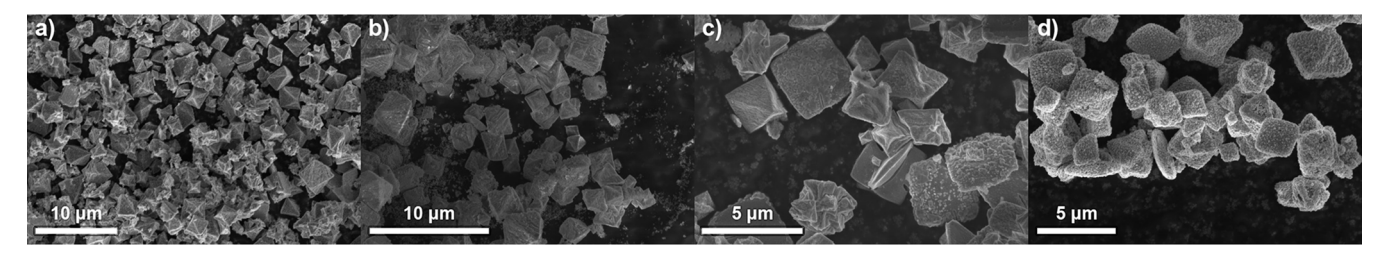


Figure 9. Demonstration of consistent morphology following thermolysis, Co–W. From left to right: (a) Co–W–Red, (b) Co–W–Ox, (c) Co–W– P_{CP} , and (d) Co–W– P_{Ox}

 ${
m Co-W-P_{ox}}$ with an $M_{{
m total}}/P$ of over 70:30. Similar to the Pd–W–P_{CP} sample, Co–W–P_{ox} was shown to be poorly crystalline; in addition to peaks consistent with unreacted CoWO₄, WO₂ formed by partial reduction of the tungstate species was also shown to be present (Figure 8). Given the amount of phosphorus incorporation seen via EDX, we argue that, unlike Pd–W–P_{ox}, Co–W–P_{ox} is a phosphide mixture with residual oxides. Co–Mo–P_{ox} is also poorly crystalline and has a much poorer $M_{{
m total}}/P$ ratio at <85:15. Notably, however, there is a noticeable peak at 17°, which better aligns with Co₂P compared to any other likely Co- or Mo-containing species. This peak is also present in Co–W–P_{ox}, but it is possibly convoluted by the CoWO₄ spectra. Phosphidation results in a roughened surface, but the general octahedral structure is maintained (Figure 9c–d).

On the other hand, Co–W–P_{CP} cleanly generated a well-defined powder pattern. The observed peaks are consistent with the formation of CoWP₂, with tungsten carbide as a minor component. CoWP₂ is consistent with the literature-reported CoNiP₂ structure, space group $P63/mmc^{41}$ (Figure 10). This ratio is consistent with EDX results with a M_{total}/P of

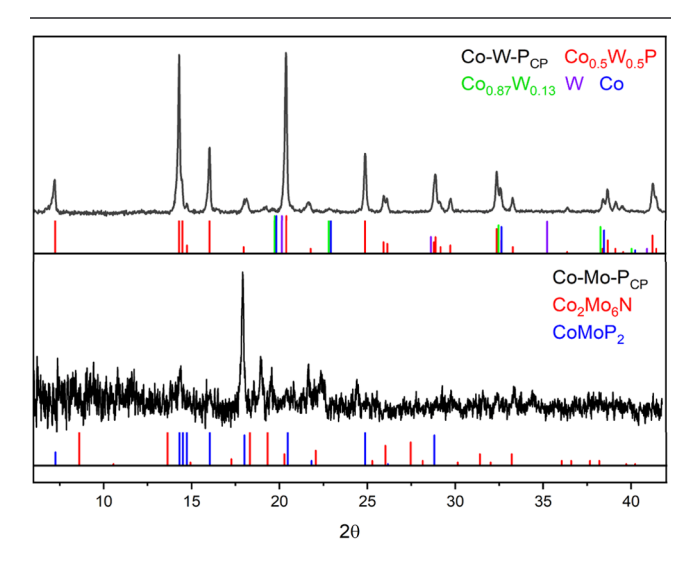


Figure 10. Comparison of coordination-polymer-derived cobalt phosphides Co-Mo- $P_{\rm CP}$ and Co-W- $_{\rm CP}$.

~55:45. This demonstrates that multimetallic tungsten phosphides can be made in relatively high crystallinity using this method. Compared to Co–W–P_{CP}, Co–Mo–P_{CP} showed considerably poorer crystallinity despite considerable phosphorus incorporation ($M_{\rm Total}/P=62:38$). Given the comparable amounts of phosphorus and poorly crystalline material, the likely product distribution(s) in this material are similar to those in the Pd–Mo–P_{CP}.

Interestingly, SEM showed that $\text{Co-Mo-P}_{\text{CP}}$, $\text{Co-W-P}_{\text{CP}}$, and $\text{Co-W-P}_{\text{Ox}}$ all retained their morphologies while heating, just with some roughening of the surface. However, $\text{Co-Mo-P}_{\text{ox}}$ had a complete collapse in morphology, eventually forming random fragments of <30 nm, which then aggregate. It is surprising that the tungsten analogue remained intact when the molybdenum system did not. One plausible explanation is that a difference in porosity between the Co-Mo-Ox and Co-W-Ox systems results in different structural integrity. Thus, as phosphine reacts with the system and further etches and roughens the surface, $\text{Co-W-P}_{\text{Ox}}$ remains intact, but $\text{Co-Mo-P}_{\text{ox}}$ collapses.

CONCLUSIONS

A pair of cyanide coordination polymers based on [M- $(CN)_8$ ⁴⁻ (M = Mo, W) representing both cyanogel systems and PBA-like systems were prepared and thermolyzed under a variety of conditions to generate an assortment of products, including metal carbides, alloy, oxides, oxide/phosphides, and phosphides. With a single exception, all of these materials are shown to maintain their morphologies after heating. The thermolytic behavior of these systems is comparable to those of hexacyanometallate systems. Treatment under argon led to the formation of metallic species, but only the cyanogel-based system made significant amounts of Mo- and W-containing alloys. In the Co-based system, metal carbide was shown to be the major $[M(CN)_8]^{4-}$ byproduct. Treatment under air generated metal oxides in all cases, but the cyanogel systems are noted for the disappearance of the $[M(CN)_8]^{4-}$ -derived element and enrichment in palladium. Attempts to generate metal phosphides from these systems showed considerable variation in effectiveness; some materials, such as the Co-W coordination polymer, cleanly gave single-phase phosphides, while most generated poorly crystalline materials or were reduced back to metallic species. Given the comparable product distributions and general behavior between octa- and hexacyanometallate compounds, it is plausible that the wide variety of known preparations and derivatizations involving 6coordinate CCPs should extend to these 8-coordinate systems as well. This provides a well-established body of literature as a starting point, possibly allowing for the rapid development of $[M(CN)_8]^{4-}$ as an important synthon for the production of a variety of Mo- and W-containing inorganic materials.

ASSOCIATED CONTENT

5 Supporting Information

The Supporting Information is available free of charge at https://pubs.acs.org/doi/10.1021/acs.chemmater.4c00834.

Sample calculations; additional IR spectra; X-ray powder pattern data; and SEM/EDX studies (PDF)

AUTHOR INFORMATION

Corresponding Author

Andrew B. Bocarsly — Department of Chemistry, Princeton University, Princeton, New Jersey 08544, United States; orcid.org/0000-0003-3718-0933; Email: bocarsly@princeton.edu

Authors

Josef A. Lawrence — Department of Chemistry, Princeton University, Princeton, New Jersey 08544, United States; orcid.org/0000-0002-5193-5282

Stephanie Dulovic — Department of Chemistry, Princeton University, Princeton, New Jersey 08544, United States; oorcid.org/0000-0003-0921-9714

Kai A. Filsinger – Department of Chemistry, Princeton University, Princeton, New Jersey 08544, United States; orcid.org/0000-0002-7061-1216

Scott B. Lee – Department of Chemistry, Princeton University, Princeton, New Jersey 08544, United States; orcid.org/0000-0003-0709-935X

Complete contact information is available at: https://pubs.acs.org/10.1021/acs.chemmater.4c00834

Author Contributions

This manuscript was written by J.A.L. and edited by A.B.B. All other authors contributed specific scientific data to the paper.

Funding

Financial support for this work was provided by Consolidated Nuclear Security LLC under Contract No. DE-NA0001942 with the United States Department of Energy (DOE). The content is solely the responsibility of the authors and does not necessarily represent the official views of the DOE or CNS.

Notes

The authors declare no competing financial interest.

ACKNOWLEDGMENTS

Dr. Vincent Lamberti is thanked for the helpful scientific discussion. The authors acknowledge the use of Princeton's Imaging and Analysis Center (IAC), which is partially supported by the Princeton Center for Complex Materials (PCCM), a National Science Foundation (NSF) Materials Research Science and Engineering Center (MRSEC; DMR-2011750).

ABBREVIATIONS

CCP –cyanide coordination polymer PBA –Prussian blue analogue

Cyanogel – cyanide coordination polymer

Co-Mo –cobalt-molybdenum

Co-W –cobalt-tungsten

Pd-Mo –palladium-molybdenum

Pd-W –palladium-tungsten

Pd-Mo-Red/Pd-W-Red –palladium-molybde-num/tungsten heated under argon

Co-Mo-Red/Co-W-Red –cobalt-molybde-num/tungsten heated under argon

Pd-Mo-Ox/Pd-W-Ox –palladium-molybde-num/tungsten heated under air

Co-Mo-Red/Co-W-Ox –cobalt-molybdenum/tungsten heated under air

Pd-Mo-P_{CP}/Pd-W-P_{CP} –coordination polymerderived palladium-molybdenum/tungsten phosphide $\label{eq:co-Mo-P} $$ Co-Mo-P_{CP} $$ \&\#x2013$; coordination polymer-derived cobalt-molybdenum/tungsten phosphide$

 $Pd-Mo-P_{Ox}/Pd-W-P_{Ox}$ –oxide-derived palladium-molybdenum/tungsten phosphide

Co-Mo-P_{Ox}/Co-W- P_{Ox} –oxide-derived cobalt-molybdenum/tungsten phosphide

REFERENCES

- (1) Ding, X.; Uddin, W.; Sheng, H.; Li, P.; Du, Y.; Zhu, M. Porous transition metal phosphides derived from Fe-based Prussian blue analogue for oxygen evolution reaction. *J. Alloys Compd.* **2020**, *814*, No. 152332.
- (2) Liu, Z.; Yang, X.; Lu, B.; Shi, Z.; Sun, D.; Xu, L.; Tang, Y.; Sun, S. Delicate topotactic conversion of coordination polymers to Pd porous nanosheets for high-efficiency electrocatalysis. *Appl. Catal., B* **2019**. 243. 86–93.
- (3) Pang, H.; Deng, J.; Du, J.; Li, S.; Li, J.; Ma, Y.; Zhang, J.; Chen, J. Porous nanocubic Mn3O4–Co3O4 composites and their application as electrochemical supercapacitors. *Dalton Trans.* **2012**, *41* (34), 10175–10181.
- (4) Zhang, L.; Lu, D.; Chen, Y.; Tang, Y.; Lu, T. Facile synthesis of Pd-Co-P ternary alloy network nanostructures and their enhanced electrocatalytic activity towards hydrazine oxidation. *J. Mater. Chem. A* **2014**, 2 (5), 1252–1256.
- (5) Liu, Z.; Yang, X.; Cui, L.; Shi, Z.; Lu, B.; Guo, X.; Zhang, J.; Xu, L.; Tang, Y.; Xiang, Y. High-Performance Oxygen Reduction Electrocatalysis Enabled by 3D PdNi Nanocorals with Hierarchical Porosity. *Part. Part. Syst. Charact.* **2018**, 35 (5), No. 1700366.
- (6) Yan, G.; Zhang, X.; Xiao, L. Prussian blue analogues-derived bimetallic phosphide hollow nanocubes grown on Ni foam as water splitting electrocatalyst. *J. Mater. Sci.* **2019**, *54* (9), 7087–7095.
- (7) Ren, J.; Meng, Q.; Xu, Z.; Zhang, X.; Chen, J. CoS2 hollow nanocubes derived from Co-Co Prussian blue analogue: Highperformance electrode materials for supercapacitors. *J. Electroanal. Chem.* **2019**, 836, 30–37.
- (8) Huang, J.; Fang, X.; Liu, X.; Lu, S.; Li, S.; Yang, Z.; Feng, X. High-Linearity Hydrogen Peroxide Sensor Based on Nanoporous Gold Electrode. *J. Electrochem. Soc.* **2019**, *166* (10), No. B814.
- (9) Oliveira, P. R.; Schibelbain, A. F.; Neiva, E. G. C.; Zarbin, A. J. G.; Marcolino, L. H.; Bergamini, M. F. Nickel hexacyanoferrate supported at nickel nanoparticles for voltammetric determination of rifampicin. *Sens. Actuators, B* **2018**, *260*, 816–823.
- (10) Wang, X.; Tan, W.; Ji, H.; Liu, F.; Wu, D.; Ma, J.; Kong, Y. Facile electrosynthesis of nickel hexacyanoferrate/poly(2,6-diaminopyridine) hybrids as highly sensitive nitrite sensor. *Sens. Actuators, B* **2018**, 264, 240–248.
- (11) Zhang, X.; Xia, M.; Liu, T.; Peng, N.; Yu, H.; Zheng, R.; Zhang, L.; Shui, M.; Shu, J. Copper hexacyanoferrate as ultra-high rate host for aqueous ammonium ion storage. *Chem. Eng. J.* **2021**, *421*, No. 127767.
- (12) Zakaria, M. B.; Li, C.; Pramanik, M.; Tsujimoto, Y.; Hu, M.; Malgras, V.; Tominaka, S.; Yamauchi, Y. Nanoporous Mn-based electrocatalysts through thermal conversion of cyano-bridged coordination polymers toward ultra-high efficiency hydrogen peroxide production. *J. Mater. Chem. A* **2016**, *4* (23), 9266–9274.
- (13) Chen, J.; Li, S.; Kumar, V.; Lee, P. S. Carbon Coated Bimetallic Sulfide Hollow Nanocubes as Advanced Sodium Ion Battery Anode. *Adv. Energy Mater.* **2017**, *7* (19), No. 1700180.
- (14) Lei, H.; Tan, S.; Ma, L.; Liu, Y.; Liang, Y.; Javed, M. S.; Wang, Z.; Zhu, Z.; Mai, W. Strongly Coupled NiCo2O4 Nanocrystal/ MXene Hybrid through In Situ Ni/Co-F Bonds for Efficient Wearable Zn-Air Batteries. ACS Appl. Mater. Interfaces 2020, 12 (40), 44639–44647.
- (15) Zhang, W.; Zhang, J.; Zhang, M.; Zhang, C.; Zhang, A.; Zhou, Y.; Tang, Y.; Wu, P. Cyano-bridged coordination polymer gel as a precursor to a nanoporous In2O3—Co3O4 hybrid network for high-capacity and cycle-stable lithium storage. *New J. Chem.* **2015**, 39 (11), 8249—8253.

- (16) Stefańczyk, O.; Majcher, A. M.; Rams, M.; Nitek, W.; Mathonière, C.; Sieklucka, B. Photo-induced magnetic properties of the [CuII(bapa)]2[MoIV(CN)8]·7H2O molecular ribbon. *J. Mater. Chem. C* 2015, 3 (33), 8712–8719.
- (17) Zakaria, M. B.; Hu, M.; Tsujimoto, Y.; Sakka, Y.; Suzuki, N.; Kamachi, Y.; Imura, M.; Ishihara, S.; Ariga, K.; Yamauchi, Y. Controlled Crystallization of Cyano-Bridged Cu—Pt Coordination Polymers with Two-Dimensional Morphology. *Chem. Asian J.* **2014**, *9* (6), 1511—1514.
- (18) Li, D.; Zheng, L.; Zhang, Y.; Huang, J.; Gao, S.; Tang, W. Coexistence of Long-Range Ferromagnetic Ordering and Glassy Behavior in One-Dimensional Bimetallic Cyano-Bridged Polymers. *Inorg. Chem.* **2003**, *42* (19), 6123–6129.
- (19) Cao, M.; Wu, X.; He, X.; Hu, C. Shape-controlled synthesis of Prussian blue analogue Co3[Co(CN)6]2 nanocrystals. *Chem. Commun.* **2005**, No. 17, 2241–2243.
- (20) Zhou, P.; Xue, D.; Luo, H.; Chen, X. Fabrication, Structure, and Magnetic Properties of Highly Ordered Prussian Blue Nanowire Arrays. *Nano Lett.* **2002**, *2* (8), 845–847.
- (21) Li, J.; Guo, M.; Yang, X.; Wang, J.; Wang, K.; Wang, A.; Lei, F.; Hao, P.; Xie, J.; Tang, B. Dual elemental modulation in cationic and anionic sites of the multi-metal Prussian blue analogue pre-catalysts for promoted oxygen evolution reaction. *Prog. Nat. Sci.: Mater. Int.* **2022**, 32 (6), 705–714.
- (22) Wu, Y.; Kong, Y.; Du, B.; Liu, T.; Ying, S.; Xiong, D.; Yi, F.-Y. Iron-Cobalt-Cerium Multimetallic Oxides Derived from Prussian Blue Precursors: Enhanced Oxygen Evolution Electrocatalysis. *ChemPlusChem* 2023, 88 (2), No. e202200422.
- (23) Du, M.; Geng, P.; Pei, C.; Jiang, X.; Shan, Y.; Hu, W.; Ni, L.; Pang, H. High-Entropy Prussian Blue Analogues and Their Oxide Family as Sulfur Hosts for Lithium-Sulfur Batteries. *Angew. Chem., Int. Ed.* **2022**, *61* (41), No. e202209350.
- (24) Hardy, D. A.; Nguyen, E. T.; Parrish, S. E.; Schriber, E. A.; Schlicker, L.; Gili, A.; Kamutzki, F.; Hohman, J. N.; Strouse, G. F. Prussian Blue Iron—Cobalt Mesocrystals as a Template for the Growth of Fe/Co Carbide (Cementite) and Fe/Co Nanocrystals. *Chem. Mater.* 2019, 31 (19), 8163—8173.
- (25) Xiao, Y.; Sun, P.; Cao, M. Core—Shell Bimetallic Carbide Nanoparticles Confined in a Three-Dimensional N-Doped Carbon Conductive Network for Efficient Lithium Storage. *ACS Nano* **2014**, 8 (8), 7846—7857.
- (26) Qi, W.; Wang, C.; Yu, J.; Adimi, S.; Thomas, T.; Guo, H.; Liu, S.; Yang, M. MOF-Derived Porous Ternary Nickel Iron Nitride Nanocube as a Functional Catalyst toward Water Splitting Hydrogen Evolution for Solar to Chemical Energy Conversion. *ACS Appl. Energy Mater.* **2022**, *5* (5), 6155–6162.
- (27) Kitchamsetti, N. A review on recent advances in Prussian blue, its analogues, and their derived materials as electrodes for high performance supercapacitors. *J. Energy Storage* **2023**, *73*, No. 108958.
- (28) Pfennig, B. W.; Bocarsly, A. B.; Prud'homme, R. K. Synthesis of a novel hydrogel based on a coordinate covalent polymer network. *J. Am. Chem. Soc.* 1993, 115 (7), 2661–2665.
- (29) Vondrova, M.; Burgess, C. M.; Bocarsly, A. B. Cyanogel Coordination Polymers as Precursors to Transition Metal Alloys and Intermetallics—from Traditional Heating to Microwave Processing. *Chem. Mater.* **2007**, *19* (9), 2203–2212.
- (30) Burgess, C. M.; Vondrova, M.; Bocarsly, A. B. A versatile chemical method for the formation of macroporous transition metal alloys from cyanometalate coordination polymers. *J. Mater. Chem.* **2008**, *18* (31), 3694–3701.
- (31) Liu, X.-Y.; Zhang, Y.; Gong, M.-X.; Tang, Y.-W.; Lu, T.-H.; Chen, Y.; Lee, J.-M. Facile synthesis of corallite-like Pt-Pd alloy nanostructures and their enhanced catalytic activity and stability for ethanol oxidation. *J. Mater. Chem. A* **2014**, 2 (34), 13840–13844.
- (32) Zhang, W.; Zhu, X.; Chen, X.; Zhou, Y.; Tang, Y.; Ding, L.; Wu, P. Cyano-bridged coordination polymer hydrogel-derived Sn–Fe binary oxide nanohybrids with structural diversity: from 3D, 2D, to 2D/1D and enhanced lithium-storage performance. *Nanoscale* **2016**, 8 (18), 9828–9836.

- (33) Fang, Z.; Zhang, A.; Wu, P.; Yu, G. Inorganic Cyanogels and Their Derivatives for Electrochemical Energy Storage and Conversion. ACS Mater. Lett. 2019, 1 (1), 158–170.
- (34) Burgess, C. M.; Yao, N.; Bocarsly, A. B. Stabilizing cyanosols: amorphous cyanide bridged transition metal polymer nanoparticles. *J. Mater. Chem.* **2009**, *19* (46), 8846–8855.
- (35) Chorazy, S.; Zakrzewski, J. J.; Magott, M.; Korzeniak, T.; Nowicka, B.; Pinkowicz, D.; Podgajny, R.; Sieklucka, B. Octacyanidometallates for multifunctional molecule-based materials. *Chem. Soc. Rev.* **2020**, *49*, 5945–6001.
- (36) Xu, K.; Yan, Y.; Ma, L.; Shen, X.; Chen, H.; Ji, Z.; Yuan, A.; Zhu, G.; Zhu, J.; Kong, L. Facile synthesis of novel tungsten-based hierarchical core-shell composite for ultrahigh volumetric lithium storage. *J. Colloid Interface Sci.* **2020**, *567*, 28–36.
- (37) Chen, Y.; Wang, Y.; Shen, X.; Cai, R.; Yang, H.; Xu, K.; Yuan, A.; Ji, Z. Cyanide-metal framework derived CoMoO4/Co3O4 hollow porous octahedrons as advanced anodes for high performance lithium ion batteries. *J. Mater. Chem. A* **2018**, *6* (3), 1048–1056.
- (38) Chen, Y.; Du, F.-H.; Lian, J.; Dong, H.; Shen, X.; Ji, Z.; Yuan, A. W-based MOF derived ZnWO4/ZnO@C hierarchical nanoflakes with superior lithium storage performance. *Ceram. Int.* **2024**, *50*, 10363–10373.
- (39) Xu, K.; Shen, X.; Ji, Z.; Yuan, A.; Kong, L.; Zhu, G.; Zhu, J. Highly monodispersed Fe2WO6 micro-octahedrons with hierarchical porous structure and oxygen vacancies for lithium storage. *Chem. Eng. J.* 2021, *413*, No. 127504.
- (40) Leipoldt, J. G.; Bok, L. D. C.; Cilliers, P. J. The Preparation of Potassium Octacyanomolybdate(IV) Dihydrate. Z. Anorg. Allg. Chem. 1974, 409 (3), 343–344.
- (41) Blanton, T.; Gates-Rector, S. The Powder Diffraction File: a quality materials characterization database. *Powder Diffr.* **2019**, 34 (4), 352–360.
- (42) Vondrova, M.; McQueen, T. M.; Burgess, C. M.; Ho, D. M.; Bocarsly, A. B. Autoreduction of Pd—Co and Pt—Co Cyanogels: Exploration of Cyanometalate Coordination Chemistry at Elevated Temperatures. *J. Am. Chem. Soc.* **2008**, *130* (16), 5563–5572.
- (43) Aparicio, C.; Machala, L.; Marusak, Z. Thermal decomposition of Prussian blue under inert atmosphere. *J. Therm. Anal. Calorim.* **2012**, *110* (2), 661–669.
- (44) Zhang, A.; Shi, H.; Liu, W.; Wang, X.; Zhou, Y.; Wu, P. Facile hydrogel-derived sub-10 nm tin—iron alloy embedded in 3D carbon nanocorals with improved cycle life and rate capability. *Ionics* **2019**, 25 (11), 5287–5295.
- (45) Liu, Q.; Li, Z.; Zhou, X.; Xiao, J.; Han, Z.; Jiang, X.; Fu, G.; Tang, Y. Cyanogel-Induced PdCu Alloy with Pd-Enriched Surface for Formic Acid Oxidation and Oxygen Reduction. *Adv. Energy Sustainability Res.* 2022, 3 (10), No. 2200067.
- (46) Gallagher, P. K.; Luongo, J. P. The thermal decomposition of K2Pt(CN)4Br2 and K2Pt(CN)4. *Thermochim. Acta* 1975, 12 (2), 159–164.
- (47) Saburi, T.; Murata, H.; Suzuki, T.; Fujii, Y.; Kiuchi, K. Oxygen Plasma Interactions with Molybdenum: Formation of Volatile Molybdenum Oxides. *J. Plasma Fusion Res.* **2002**, *78* (1), 3–4.
- (48) Habainy, J.; Iyengar, S.; Surreddi, K. B.; Lee, Y.; Dai, Y. Formation of oxide layers on tungsten at low oxygen partial pressures. *J. Nucl. Mater.* **2018**, *506*, 26–34.
- (49) Wei, X.; Song, Y.; Song, L.; Liu, X. D.; Li, Y.; Yao, S.; Xiao, P.; Zhang, Y. Phosphorization Engineering on Metal—Organic Frameworks for Quasi-Solid-State Asymmetry Supercapacitors. *Small* **2021**, 17 (4), No. 2007062.